ACS APPLIED MATERIALS & INTERFACES

Research Article

www.acsami.org

Highly Exothermic and Superhydrophobic Mg/Fluorocarbon Core/Shell Nanoenergetic Arrays

Xiang Zhou,[†] Daguo Xu,[†] Guangcheng Yang,[‡] Qiaobao Zhang,[†] Jinpeng Shen,[‡] Jian Lu,[†] and Kaili Zhang*[,†]

[†]Department of Mechanical and Biomedical Engineering, City University of Hong Kong, 83 Tat Chee Avenue, Kowloon, Hong Kong

[‡]Institute of Chemical Materials, China Academy of Engineering Physics, Mianyang 621900, Sichuan, China

Supporting Information

ABSTRACT: Mg/fluorocarbon core/shell nanoenergetic arrays are prepared onto silicon substrate, with Mg nanorods as the core and fluorocarbon as the shell. Mg nanorods are deposited by the glancing angle deposition technique, and the fluorocarbon layer is then prepared as a shell to encase the Mg nanorods by the magnetron sputtering deposition process. Scanning electron microscopy and transmission electron microscopy show the core/shell structure of the Mg/fluorocarbon arrays. X-ray energy-dispersive spectroscopy, X-ray diffraction, and Fourier transform infrared spectroscopy are used to characterize the structural composition of the Mg/fluorocarbon. It is found that the as-prepared fluorocarbon layer consists of shorter molecular chains compared to that of bulk polytetrafluoroethylene, which is proven beneficial to the low onset reaction temperature of Mg/fluorocarbon. Water contact angle test demonstrates the superhydrophobicity of the Mg/fluorocarbon arrays, and a static contact angle as high as 162° is achieved. Thermal analysis shows that the Mg/fluorocarbon material exhibits a very low onset reaction temperature of about 270 °C as well as an ultrahigh heat of reaction approaching 9 kJ/g. A preliminary combustion test reveals rapid combustion wave propagation, and a convective mechanism is adopted to explain the combustion behaviors.

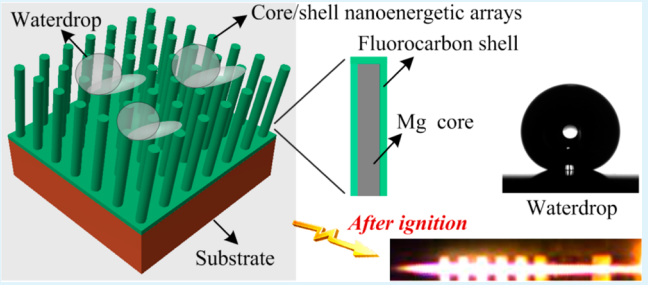

KEYWORDS: *Mg/fluorocarbon, core/shell, nanoenergetic arrays, superhydrophobicity, ultrahigh heat of reaction*

1. INTRODUCTION

Nanoenergetic materials (nEMs) have received steadily growing interest because of the improved performance in ignition, combustion, and energy release.[1−4] They have broad potential applications in both civilian and military fields, including microignition and rapid initiation,[5−7] gas generators,[8,9] microactuation,[10,11] burn rate modifiers,[12,13] synthesis and processing of materials,[14,15] and biomedicine-related applications.[16,17] Ultrasonic mixing of nanoscale fuel and oxidizer particles is widely employed as an efficient way to prepare nanoenergetic composites. However, the passivation shell around the nanometal behaves as a noticeable "dead weight" (especially for particle diameters < 50 nm), which will decrease the energy density as well as inhibit combustion propagation.[18,19] Moreover, the nonhomogeneous distribution of fuel and oxidizer can cause scattering in the ignition and combustion performance.[2] Therefore, efforts are made to obtain nanostructured energetic composites, in which the distribution and contact conditions of fuel and oxidizer will be greatly improved for better performance.[4] Various methods have been developed to prepare nanostructured energetic composites, mainly including layered vapor deposition,[20,21] sol−gel technique,[22,23] arrested reactive milling,[24,25] self-assembly,[26,27] porous silicon with oxidizers embedded,[28,29] and nanowires/rods-based core/shell structure.[30,31] Nanostructured energetic composites have already shown many promising prospects, e.g., self-assembled nanothermites exhibit enhanced heat-release rate and higher combustion wave speed than those of nanocomposites made by simply ultrasonic mixing,[32,33] and core/shell CuO/Al displays greatly improved mixing uniformity and reduced activation energy compared to those of nanoparticle-based thermite.[34]

Although much research has been carried out in the field of nanostructured energetic composite, two main limitations still exist. First, the formulations for nanoenergetic composites are mostly based on thermite reactions (e.g., Al/CuO,[21,27,30,32,34−36] Mg/CuO,[37] Al/Fe_2O_3,[33,38] and Al/Co_3O_4[31]) and intermetallic reactions (e.g., Al/Ni[7,39]). However, the theoretical heats of reaction are not very high for these formulations (usually <5 kJ/g),[40] and it is practically difficult to reach the theoretical value. Some oxidizers are capable of high heat of reaction with metals, but they are usually hygroscopic (e.g., $NaClO_4·H_2O$). Second, the research is deficient in probing the resistance of nanoenergetic composite to variable

Received: April 5, 2014
Accepted: June 11, 2014
Published: June 11, 2014

environmental conditions. Nanometric metals oxidize easily in atmospheric air and can even react with cold water spontaneously.[37] Some widely used oxidizers are hydrophilic (e.g., CuO) or even hygroscopic, which makes performance maintenance a big issue. It was reported that after treating MoO_3 nanoparticles in 99% relative humidity atmosphere for 1 day, the Al/MoO_3 nanocomposite exhibited a reduction in burn velocity of over 99%.[41] The humidity of air differs according to locations and climates. Consequently, concerns arise in that while the freshly prepared nanocomposites are capable of superior properties, the performance can degrade significantly after long-distance transportation and/or long-term storage.

We developed Mg/CuO nanoenergetic arrays which exhibit improved long-term storage stability in dry air.[37] In this work, we prepare Mg/fluorocarbon nanoenergetic arrays with the Mg nanorods as core and the fluorocarbon as shell as illustrated in Figure 1. Mg nanorods are first deposited by the glancing angle

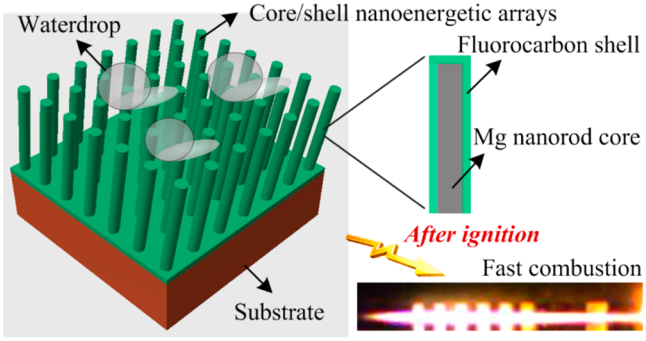

Figure 1. Schematic drawing of Mg/fluorocarbon core–shell nanoenergetic arrays with both superhydrophobic feature and highly exothermic property.

deposition technique, and then the fluorocarbon is deposited around the Mg nanorods by magnetron sputtering of polytetrafluoroethylene (PTFE) target. Reaction between Mg and PTFE enables high heat release according to eq 1, with an ultrahigh theoretical heat of reaction (9.6 kJ/g) calculated from the thermodynamic data.[42] Besides heat release, PTFE-rich mixtures are also expected to promote gas generation, which is beneficial for many applications[10,43,44] and distinguishes them from most thermite and intermetallic reactions. Also, one potential advantage lies in that, when used in atmospheric conditions, the reaction product carbon can readily react with oxygen in the air to contribute more energy release and gas generation.

$$n\mathrm{Mg} + (\mathrm{C_2F_4})_n \rightarrow 2n\mathrm{MgF_2} + 2n\mathrm{C};\ \Delta H = -9.6\ \mathrm{kJ/g} \quad (1)$$

Moreover, PTFE is very stable in normal environmental conditions, resistant to acid and alkali, and hydrophobic, making it an excellent candidate to ensure long-term storage stability when used as the shell of nanometric metals. On the basis of the Wenzel model and/or Cassie–Baxter model, it has also been demonstrated that when hydrophobic material is deposited onto nanotextures, a superhydrophobic surface will form.[45−47] Therefore, highly exothermic and superhydrophobic nanoenergetic arrays are conceived, which will promisingly resist the variable environmental conditions and, accordingly, preserve the high performance for an extended period.

2. EXPERIMENTAL SECTION

One-hHalf of a 4-in. silicon wafer is cleaned in acetone with ultrasonic vibration. It is then rinsed by deionized water and blown dry in air. Mg nanorods are prepared in a similar way as indicated in the previous paper.[37] Briefly speaking, Mg nanorods are deposited onto the silicon substrate by glancing angle thermal evaporation. The incident angle of Mg vapor flux with respect to the substrate surface normal is fixed at 84°, and the average distance between the substrate and the evaporation source is 8 cm. The thickness of Mg nanorods prepared in this work is consistently set to be nominal 1 μm as calibrated on a horizontally positioned silicon substrate. Fluorocarbon is then deposited around the as-prepared Mg nanorods by RF magnetron sputtering process. The equipment is JunSun MGM-600 sputtering system, and the PTFE target is 2 in. in diameter and 0.125 in. in thickness. The base vacuum and working pressure are 1.6×10^{-6} and 1.1×10^{-3} Torr, respectively. Argon gas is used as the working atmosphere, with a flow rate of 50 sccm. The sputtering power is 140–145 W.

The as-prepared Mg nanorods and Mg/fluorocarbon nanoenergetic arrays are directly observed with a field emission scanning electron

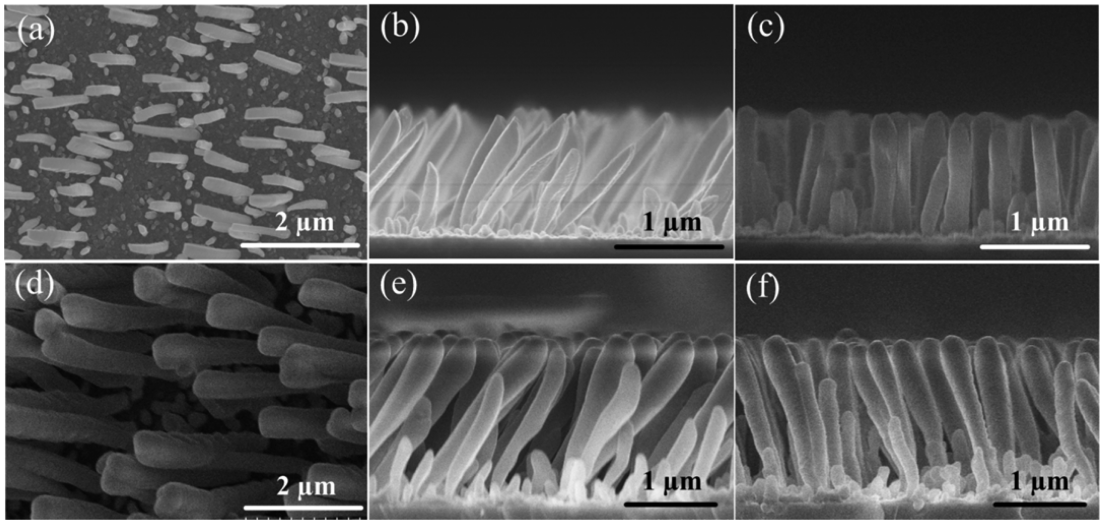

Figure 2. SEM images of (a–c) Mg nanorods and (d–f) Mg/fluorocarbon nanoenergetic arrays. (a, d) Top-view images of Mg nanorods and Mg/fluorocarbon. (b, e) Cross-sectional images from the direction parallel to the Mg vapor flux. (c, f) Cross-sectional images from the direction vertical to the Mg vapor flux.

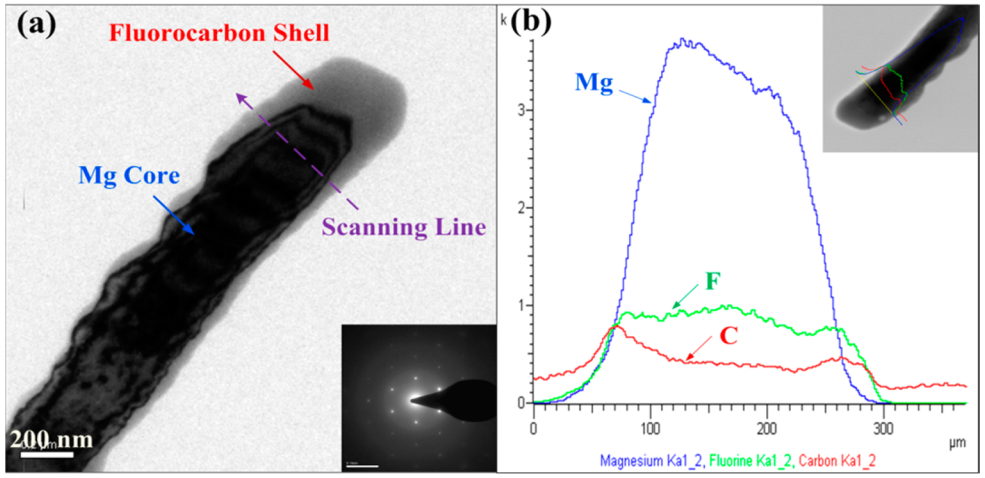

Figure 3. (a) TEM image of the Mg/fluorocarbon core/shell structure (inset shows the selected area electron diffraction image). (b) EDS line-scan analysis result (inset shows the location of the scanning line).

microscope (FESEM, Hitachi S4800). A transmission electron microscope (TEM, FEI Tecnai G2 20) is employed to check the core/shell structure of the Mg/fluorocarbon. X-ray diffraction (XRD, RigakuSmartLab), X-ray energy-dispersive spectrometry (EDS, Oxford Instruments, INCAx-sight EDS Detectors with INCA Energy TEM Software), and Fourier transform infrared spectroscopy (FTIR, Bruker Tensor 27) are used to identify the structural composition of the Mg/fluorocarbon. XRD is also used to analyze the composition of the reaction product after thermal analysis. Mg/fluorocarbon is scraped from the silicon substrate for FTIR characterization. The FTIR spectrum is collected by cumulating 16 scans at a resolution of 4 cm^{-1}, and the absorption spectrum of bulk PTFE target is also obtained for comparison.

The deposition rate of fluorocarbon on the Mg nanorods is different from that on a horizontally positioned substrate, and it is difficult to determine the rate accurately. Therefore, in this work, nominal thickness is used to describe the theoretical thickness of fluorocarbon based on the deposition rate on a horizontally positioned silicon substrate. By depositing nominal 175, 300, and 420 nm fluorocarbon around a constant batch of Mg nanorods, three kinds of Mg/fluorocarbon nanoenergetic arrays are prepared. These three types of samples are compared in terms of superhydrophobicity and heat-release properties.

Mg/fluorocarbon nanoenergetic arrays on silicon are directly used for static contact angle tests. The contact angle of a sessile drop is measured by a Ramé-Hart model 500 Advanced Goniometer attached to a CCD camera (30 fps) using DROP image software, and a deionized water droplet with a volume of 5 μL is used. Mg/fluorocarbon is scraped from the substrate for thermal analysis. Differential scanning calorimetry (DSC, TA Instruments Q20) and differential thermal/thermogravimetric analysis (DTA-TG, TA Instruments Q600) are performed to analyze the heat-release properties of the materials. DSC tests are conducted for three kinds of samples (sample masses are 2.5−3.5 mg). DTA-TG tests are made for bulk PTFE material (cut from target with a sample mass of 19.6 mg) and Mg/fluorocarbon with a nominal fluorocarbon thickness of 420 nm (sample mass is 3.7 mg). DSC analyses are conducted from 40 to 680 °C with a heating rate of 5 °C/min under 75 mL/min Ar flow. DTA-TG tests are run from 40 to 800 °C with a heating rate of 10 °C/min under 100 mL/min Ar flow. To obtain a stable Ar atmosphere, Ar flow is started 40 min before increasing the temperature in both DTA-TG and DSC tests. Universal analysis 2000 software is used to process the thermal analysis data. A preliminary combustion test is also performed, and details are given in section 3.5.

3. RESULTS AND DISCUSSION

3.1. SEM, TEM, and EDS Characterization. Figure 2 shows SEM images of Mg nanorods and Mg/fluorocarbon nanoenergetic arrays. Figure 2a and 2d shows the top-view images of Mg nanorods and Mg/fluorocarbon, respectively. Figure 2b and 2e shows the cross-sectional views of Mg nanorods and Mg/fluorocarbon, respectively, from the direction parallel to the Mg vapor flux. Figure 2c and 2f is the cross-sectional images from the direction normal to the Mg vapor flux. Growth of Mg nanorods is dominated by atomic shadowing and adatom diffusion mechanisms.[48] As can be seen from Figure 2a−c, Mg nanorods obtained are similar to those reported before.[49] Mg nanorods with an average diameter of about 150−200 nm have been prepared, and the nanorods exhibit a nearly equal diameter from the base to the top. After deposition of nominal 500 nm thick fluorocarbon, the as-prepared Mg/fluorocarbon shows increased diameter and length as can be seen in Figure 2d−f. The diameter of Mg/fluorocarbon decreases gradually from the top to the base. However, due to the high kinetic energies of the ejected particles by sputtering, fluorocarbon can still coat the base of the Mg nanorods. The topography of the fluorocarbon is a continuous layer rather than the aligned columns obtained for CuO shell,[37] which is believed to further increase the resistance of the metal core to oxidation.

Figure 3 shows a typical TEM image of the Mg/fluorocarbon core/shell structure (Figure 3a) as well as the EDS line-scan analysis result (Figure 3b). The Mg/fluorocarbon for testing is prepared by depositing nominal 175 nm fluorocarbon on Mg nanorods. As can be seen from Figure 3a, the fluorocarbon appears as a continuous layer, which corresponds to the SEM observation. The thickness of the fluorocarbon on the top of the Mg nanorod is about 200 nm; however, the fluorocarbon on the side wall of the Mg nanorod is much thinner, which is why the "nominal thickness" is used to describe the dimension of the fluorocarbon. The inset in Figure 3a shows the hexagonal compact structure of the single-crystal Mg nanorod.[37,49] EDS line-scan analysis is carried out to identify further the elemental composition and distribution of the Mg/fluorocarbon. The location of the scanning line is shown in the inset of Figure 3b, and it is also marked in Figure 3a with a dashed line for clarity (scanning is along the arrow direction). C, F, and Mg elements are identified, corresponding to the fluorocarbon layer and Mg

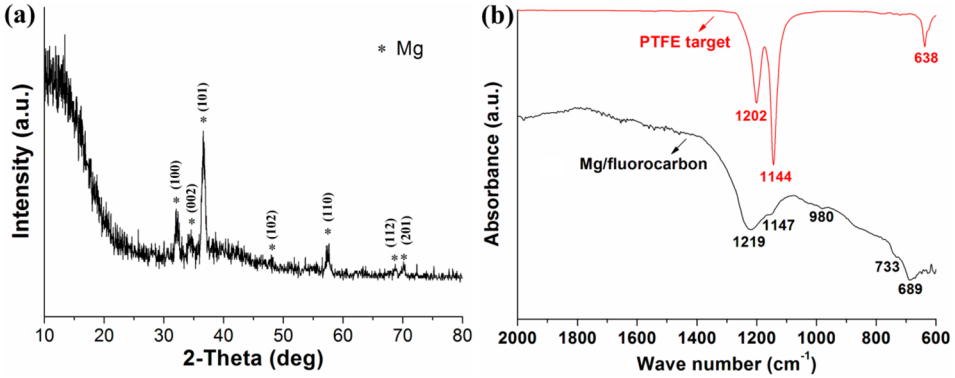

Figure 4. (a) XRD pattern of the Mg/fluorocarbon. (b) FTIR spectra of the bulk PTFE and Mg/fluorocarbon.

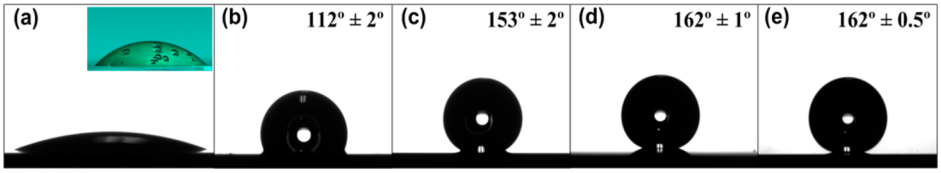

Figure 5. WDCA tests for different surfaces: (a) Mg nanorods after 2 min of spreading (inset shows the reaction between the Mg nanorods and cold water drop); (b) 500 nm-thick fluorocarbon film; (c–e) Mg/fluorocarbon nanoenergetic arrays with different nominal fluorocarbon thicknesses of (c) 420, (d) 300, and (e) 175 nm.

nanorod. No O is detected, indicating that Mg nanorods are protected by the fluorocarbon shell effectively. It should be mentioned that Mg nanorods oxidize readily to form a trace of MgO when taken out of the vacuum chamber.[37] However, the following deposition of fluorocarbon protects the Mg nanorods from continuously oxidizing. As the amount of nascent MgO is very few, O cannot be detected. The amounts of C and F in the periphery are higher than that of Mg because of the coating effect (the right-hand edge of the curves in Figure 3b); however, as the fluorocarbon layer is very thin at some location, an almost simultaneous rise of F and Mg signals is also found (left-hand edge of the curves in Figure 3b). The background signal of C is not zero, which is due to the carbon-coated copper grid.

3.2. XRD and FTIR Characterizations. Figure 4 shows the XRD (Figure 4a) and FTIR (Figure 4b) characterization results of the Mg/fluorocarbon, and the FTIR pattern of bulk PTFE is also presented as reference. Mg/fluorocarbon with a fluorocarbon nominal thickness of 300 nm is prepared for test. Only the characteristic peaks of metallic Mg appear in Figure 4a, indicating that no obvious prereaction happens during the deposition of fluorocarbon, and the fluorocarbon shell is amorphous. It is also found that although each Mg nanorod is single crystal, the growth directions of the massive Mg nanorods are not identical, leading to multiple diffraction peaks in the XRD pattern, and a similar result has been reported before.[49] Results from EDS can only prove the existence of C and F elements in the samples; therefore, FTIR is employed as an effective tool to analyze further the composition of the Mg/fluorocarbon. As Mg has no infrared activity, the FTIR spectrum of Mg/fluorocarbon actually reflects the composition of the fluorocarbon shell. The FTIR spectrum of bulk PTFE target shows the characteristic absorption bands of the CF_2 groups at wavenumbers of 638, 1144, and 1202 cm^{-1}, which can be attributed to the rocking vibration, asymmetric stretching vibration, and symmetric stretching vibration of the CF_2 groups, respectively.[50,51] As for the Mg/fluorocarbon sample, these three vibration modes still exist but with wavenumbers blue shifted slightly. Another peculiarity for Mg/fluorocarbon is the appearance of absorption bands at wavenumbers of 733 and 980 cm^{-1}, which can be ascribed to the vibration of CF_3.[50,52] CF_3 groups only exist at the end of the molecular chain, so the appearance of CF_3 vibration demonstrates the shorter length of molecular chains for fluorocarbon. Shorter molecular chains can make the thermal property of fluorocarbon differ from that of the bulk PTFE, and the following thermal analyses verify it.

3.3. Water Drop Contact Angle Test. Water drop contact angle (WDCA) test results are shown in Figure 5. When a drop of deionized water (25 °C) is placed directly onto the Mg nanorods, it spreads gradually. During the extending process, the water drop reacts with the highly reactive Mg nanorods, with many bubbles generated as shown in the inset of Figure 5a (the picture is taken from another optical microscope). The WDCA test result of Mg nanorods surface after 2 min of spreading is shown in Figure 5a. The static contact angles for 500 nm thick fluorocarbon film is 113° (fluorocarbon is deposited directly onto the flat silicon substrate), which is similar to that reported before (about 105°).[52] Remarkably, when the fluorocarbon is deposited around Mg nanorods, the contact angle of the as-prepared nanoenergetic arrays increases profoundly to over 150°, which proves our design concept of superhydrophobicity. Contact angle reaches 153° for Mg/fluorocarbon with a nominal fluorocarbon thickness of 420 nm, and the value increases further to 162° when the nominal thickness of fluorocarbon decreases to 300 or 175 nm. The water drop can even roll down automatically when the nominal thickness of fluorocarbon is 175 nm (videos of WDCA tests for three kinds of Mg/fluorocarbon can be seen in the Supporting Information), and the reason for this phenomenon lies in the contact angle hysteresis. The contact angle hysteresis is measured to be as small as 0.7° when the nominal thickness of fluorocarbon is 175 nm, and smaller contact angle hysteresis leads to less drag force and easier drop moving.[53] Two models

are usually employed to correlate surface roughness with the apparent contact angle, namely, the Wenzel and Cassie−Baxter models. It was stated that increasing the aspect ratio of the surface texture favored the occurrence of Cassie−Baxter wetting condition, which led to easy roll off of water droplets.[47] On the basis of the nanorod structure and small contact angle hysteresis obtained in this work, Cassie−Baxter mode can be used to explain the experimental results. In general, the prepared Mg/fluorocarbon nanoenergetic arrays manifest excellent superhydrophobic property, which is expected to enhance the resistance of nanoenergetic material to the complex and variable environmental conditions, and the Mg/fluorocarbon can even be considered as an underwater energy source.

3.4. Thermal Analysis. Thermal analysis results are shown in Figure 6. Figure 6a and 6b shows the DTA-TG curves of the bulk PTFE and Mg/fluorocarbon nanoenergetic arrays with a nominal fluorocarbon thickness of 420 nm, respectively. Figure 6c displays the DSC curves of three kinds of Mg/fluorocarbon nanoenergetic arrays with different nominal fluorocarbon thickness of 175 (sample 1), 300 (sample 2), and 420 nm (sample 3).

As can be seen from Figure 6a, there are two endothermic peaks in the DTA curve for the bulk PTFE material. The first one starts at about 314 °C, corresponding to the melting process of PTFE; the second one begins at 525 °C, which coincides with the rapid mass loss in the TG curve, indicating the decomposition process of PTFE. Eventually, PTFE decomposes to gas products totally. Unlike that of bulk PTFE material, fluorocarbon film begins to decompose gradually from about 200 °C as indicated by the weight loss curve in Figure 6b. FTIR characterization reveals the shorter molecular chains of the prepared fluorocarbon layer compared to that of bulk PTFE, which means that the number of C−C bonds is reduced in fluorocarbon and, consequently, less energy is required to break these bonds to generate the gaseous reactant CF_2. Therefore, the decomposition temperature of fluorocarbon is much lower than that of bulk PTFE. The theoretical values are listed in Table 1. They are calculated from the data of standard heats of formation.[42] The DTA curve of the Mg/fluorocarbon in Figure 6b shows a broad exothermic peak, and 40% of the original mass is lost after the reaction, indicating that much gas can be generated if the amount of fluorocarbon is excessive. It is conceivable that heat release and gas generation can be adjusted by changing the mass ratio of Mg to fluorocarbon. More detailed information on heat-release properties can be obtained from Figure 6c, and the results are summarized in Table 1.

Generally, these three samples all exhibit a similar low onset reaction temperature of about 270 °C as well as two separated exotherms, while the first main exotherm is composed of several superimposed exothermic peaks. Probably because of the unavailability of commercial Mg nanoparticles, we cannot find a relevant report of a thermal analysis of Mg/PTFE nanocomposite. However, the heat flow patterns obtained here are quite different from those of n-Al/n-PTFE reactive composites, in which a small preignition reaction was found in the temperature range of about 400−500 °C followed by a stronger exothermic peak located at 500−600 °C.[54,55] Due to the reduced decomposition temperature of the fluorocarbon compared to that of bulk PTFE, the onset reaction temperature is significantly decreased for the prepared Mg/fluorocarbon. Samples 1 and 2 show similar heat flow patterns with the first

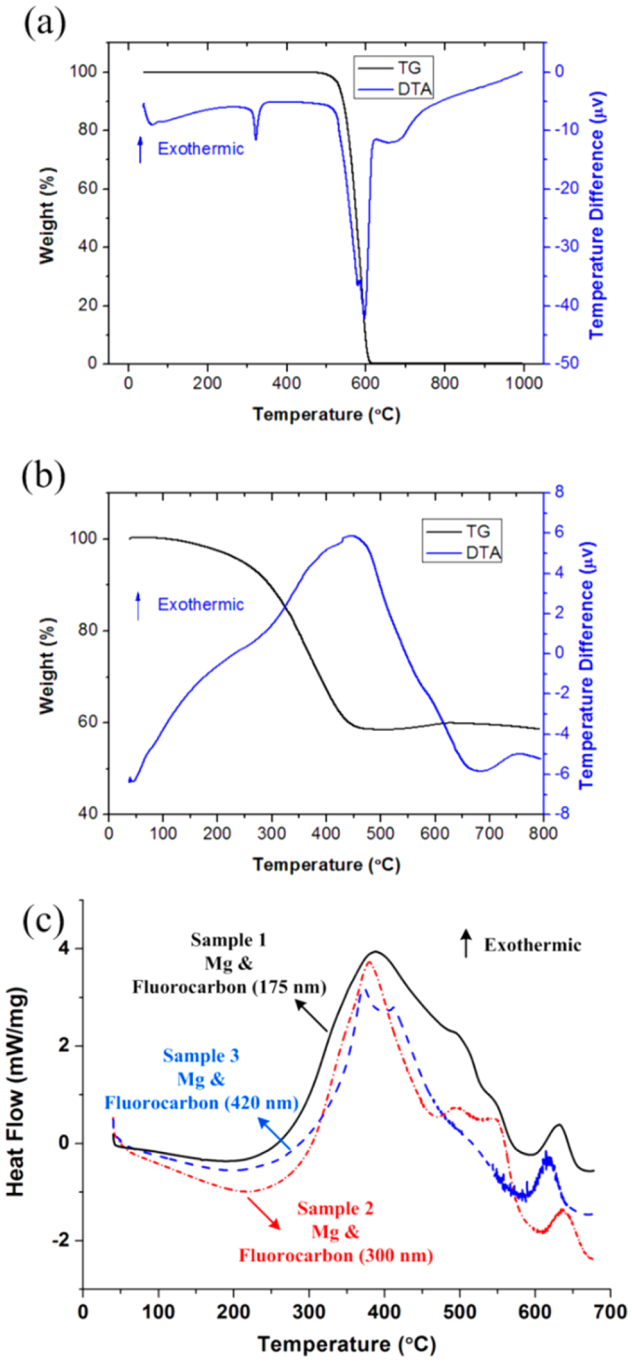

Figure 6. Thermal analysis results. (a) DTA-TG plot for bulk PTEF. (b) DTA-TG plot for Mg/fluorocarbon (nominal fluorocarbon thickness is 420 nm). (c) DSC plots for three kinds of Mg/fluorocarbon materials.

main exotherm composed of three superimposed peaks; however, it is not the case for sample 3. Integration of the heat flow curve gives the heat of reaction, and again, samples 1 and 2 exhibit comparable values of total heat release, which are higher than that of sample 3. On the other hand, three kinds of samples show similar heats of reaction for the second small exothermic peak. It is speculated that the ideal stoichiometric ratio for Mg/fluorocarbon lies between those of samples 1 and 2, while the mass of fluorocarbon is evidently excessive for sample 3. Although a detailed analysis of the reaction process is not available at present, the highly exothermic property of our

Table 1. Measured Heats of Reaction for Different Mg/Fluorocarbon Compositions and Calculated Theoretical Heat-Release Values for Mg/PTFE

	heat release of the first exotherm (kJ/g)	heat release of the second exotherm (kJ/g)	total heat of reaction (kJ/g)
Mg/fluorocarbon			
sample 1 (fluorocarbon nominal thickness 175 nm)	8.650	0.335	8.985
sample 2 (fluorocarbon nominal thickness 300 nm)	8.416	0.282	8.698
sample 3 (fluorocarbon nominal thickness 420 nm)	6.347	0.320	6.667
theoretical heat release (under ideal stoichiometry ratio)			
Mg/PTFE			9.6

new Mg/fluorocarbon material is proven undoubtedly, and the heat of reaction of about 9 kJ/g is much higher than those reported previously based on metal/metal oxide materials.[21,30,31,35,40] Figure 7 shows the XRD pattern of the reaction

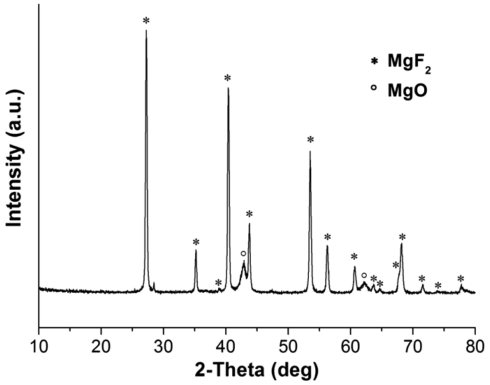

Figure 7. XRD pattern of the reaction products after thermal analysis. Reaction products are reclaimed from sample 2 after DSC test (scanned to 680 °C).

products of sample 2 after DSC test. MgF_2 peaks are obvious, but another theoretical product carbon does not appear, which is probably due to the amorphous structure of the product carbon. Slight MgO peaks are also detected, which can result from oxidation of Mg nanorods by the trace oxygen in the sample cell.

3.5. Preliminary Combustion Test. Thermal analysis can be used to characterize the potential energetic capability of energetic materials, while combustion performance is indicative of the reactive power which is also very important for practical applications. Mg/fluorocarbon with a nominal fluorocarbon thickness of around 300 nm is prepared for the combustion test. The Mg/fluorocarbon nanocomposite (sample mass 3.3 mg) is scraped from the silicon substrate and then loaded into an open-ended glass capillary tube. The diameter of the tube is 1.1 mm, and the length is 10 cm, but the loading area is only the rightmost 1.8 cm of the capillary tube. The sample is ignited from one end of the capillary tube by an electric spark igniter which is commercially available, and then the combustion flame self-propagates throughout the tube. The combustion propagation process is recorded by a high-speed camera (Photron FASTCAM-APX RS2), which is remotely controlled by a laptop. The sampling rate is 100 000 frames per second with a frame size of about 256 × 32 pixels. The aperture value is adjusted to 2.8 to reduce the light into the high-speed camera, so that the reaction front edges are discernible for speed measurement. The set of experimental apparatus is shown schematically in Figure 8.

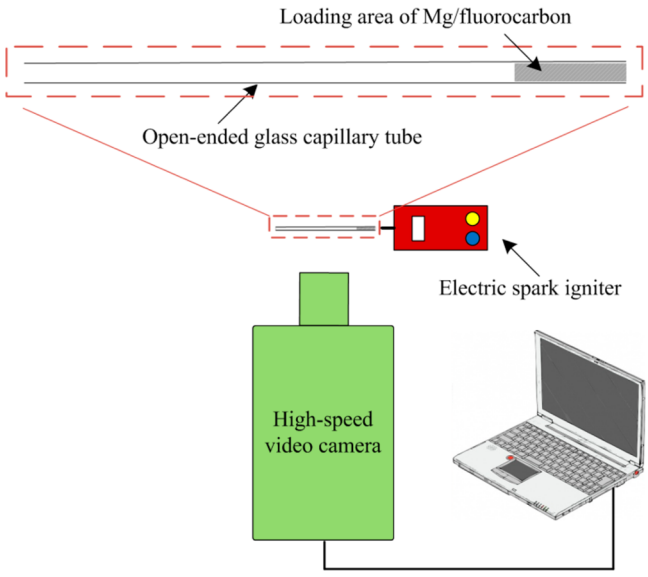

Figure 8. Schematic diagram of the set of experimental apparatus for recording combustion flame propagation.

Figure 9 shows the flame propagation in a capillary tube, and the time interval between the successive two frames is 10 μs. A

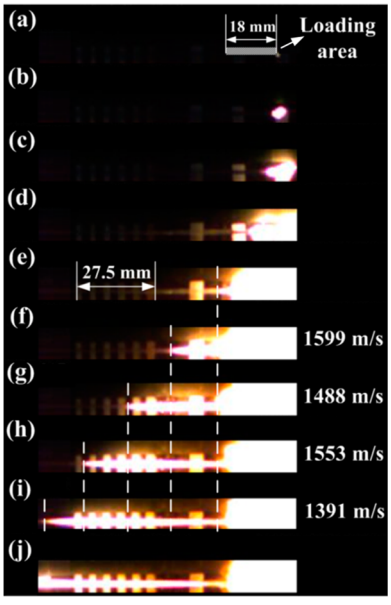

Figure 9. Combustion front propagation of the Mg/fluorocarbon nancomposites.

video has been made by compiling the sequential photos to present the combustion process intuitively, and it can be obtained in the Supporting Information. Many factors affect the combustion velocities of nanoenergetic composites in a tube, such as the tube diameter, the loading density of nanocomposites, and the stoichiometric ratio of fuel to oxidizer. The loading density is often described as the percentage of

theoretical maximum density (% TMD), and the TMD is calculated as the weighted average value of respective components. For the Mg/fluorocarbon nanocomposites prepared in this work, bulk densities of Mg (1.738 g/cm^{-3}) and PTFE (2.2 g/cm^{-3}) are approximately assigned for Mg nanorods and fluorocarbon, respectively, and MgO is not considered in the composition. Exact stoichiometry between the Mg and the fluorocarbon is unknown; however, two extreme conditions can be considered, namely, 100% Mg and 100% fluorocarbon. Consequently, the TMD of Mg/fluorocarbon can be estimated as among 1.738−2.2 g/cm^{-3}. The actual loading density is calculated as the loading mass (3.3 mg) divided by the loading volume (17.1 mm^{-3}), which turns out to be 0.193 g/cm^{-3}. On the basis of the conditions discussed above, the loading density can be expressed as within 8.8−11.1% TMD. A convective propagation mechanism was proposed to be dominant for nanocomposites with loading densities in this range, and combustion velocities on the order of hundreds of meters per second were typically reported.[19,56−58] A melt dispersion mechanism has also been proposed for an explanation of fast reaction rates and high flame front velocities of nanothermites, in which it was proposed that the atomic scale liquid metal clusters dispersed into the oxidizer with a high speed. However, the mechanism was said to be suitable for nanocomposites with spherical metal nanoparticles as component,[59,60] which is not the case in this study as Mg possesses nanorod-like morphology.

The loading area is labeled in Figure 9a, which lies in the rightmost space of the capillary tube. Mg/fluorocarbon reacts violently after ignition, with a combustion front propagating across the tube very fast. The capillary tube is totally shattered after the combustion process, indicating that much gas has been generated promptly. The reaction zone is highly luminous, and it is difficult to identify the combustion front edges accurately in the initial loading areas. However, the average combustion wave velocity through the loading area can be roughly estimated to be around 450−600 m/s from the combustion frames (assuming 3 or 4 frames for the flame propagating through), which demonstrates the good combustion performance of the Mg/fluorocarbon. The magnitude of velocity is consistent with the results published before.[19,56−58] It is also found that the combustion wave continuously propagates along the tube where there is no nanocomposites originally, and this observation supports the convective propagation mechanism, in which the convective gases resulted from the exothermic reaction propel the reaction media forward in an extremely fast speed. The combustion wave is relatively stable, and the wave fronts are clear in this region, which are indicated by dashed lines in the photos. The distance between the adjacent dashed lines is measured according to the reference length scale (rectangular white paper array is prepositioned as the length reference), and then the combustion front velocity can be calculated readily. A combustion wave velocity as high as about 1500 m/s is determined in this area. The higher combustion wave speed in this region can be attributed to the much lower "loading density" compared with that of the initial loading area, which means that the convective gases can move forward with much less resistance. It is also possible that the 1.8 cm loading length is too short to achieve stable combustion wave propagation; in other words, the combustion velocity may continue to increase if the loading area is longer.

4. CONCLUSIONS

Mg/fluorocarbon nanoenergetic arrays are prepared and investigated in terms of energetic properties and wettability in this study. The shorter molecular chain of the prepared fluorocarbon compared with that of bulk PTFE is beneficial to decomposition of fluorocarbon to gaseous species, which further promotes the low onset reaction temperature of Mg/fluorocarbon. The prepared Mg/fluorocarbon nanoenergetic arrays exhibit fascinating superhydrophobic property, which is believed to enhance the resistance to the changeable environmental conditions so as to improve the long-term storage stability. The superhydrophobic Mg/fluorocarbon can even be envisioned as an underwater energy source. Thermal analysis results demonstrate the excellent energetic capability of the Mg/fluorocarbon. The high heat release and available gas generation indicate very promising application potentials such as microactuation/micropropulsion. An initial combustion test has already shown the rapid combustion wave velocity, which is indicative of the high reactive power. We expect that the new Mg/fluorocarbon nanoenergetic arrays introduced in this work will contribute to the research of nanostructured energetic composite, and the design concept adopted here can be further extended by the engineering community to advance development of this field.

■ ASSOCIATED CONTENT

Ⓢ Supporting Information

Videos of WDCA tests; video of combustion flame propagation in the glass capillary tube. This material is available free of charge via the Internet at http://pubs.acs.org.

■ AUTHOR INFORMATION

Corresponding Author

*E-mail: kaizhang@cityu.edu.hk.

Notes

The authors declare no competing financial interest.

■ ACKNOWLEDGMENTS

This work was supported by NSAF (grant no. U1330132).

■ REFERENCES

(1) Rossi, C.; Zhang, K.; Estève, D.; Alphonse, P.; Tailhades, P.; Vahlas, C. Nanoenergetic Materials for MEMS: A Review. *J. Microelectromech. Syst.* **2007**, *16*, 919−931.

(2) Dreizin, E. L. Metal-Based Reactive Nanomaterials. *Prog. Energy Combust. Sci.* **2009**, *35*, 141−167.

(3) Dlott, D. D. Thinking Big (and Small) about Energetic Materials. *Mater. Sci. Technol.* **2006**, *22*, 463−473.

(4) Zhou, X.; Torabi, M.; Lu, J.; Shen, R.; Zhang, K. Nanostructured Energetic Composites: Synthesis, Ignition/Combustion Modeling, and Applications. *ACS Appl. Mater. Interfaces* **2014**, *6*, 3058−3074.

(5) Zhou, X.; Shen, R.; Ye, Y.; Zhu, P.; Hu, Y.; Wu, L. Influence of Al/CuO Reactive Multilayer Films Additives on Exploding Foil Initiator. *J. Appl. Phys.* **2011**, *110*, 094505.

(6) Zhang, K.; Rossi, C.; Petrantoni, M.; Mauran, N. A Nano Initiator Realized by Integrating Al/CuO-Based Nanoenergetic Materials With a Au/Pt/Cr Microheater. *J. Microelectromech. Syst.* **2008**, *17*, 832−836.

(7) Morris, C. J.; Mary, B.; Zakar, E.; Barron, S.; Fritz, G.; Knio, O.; Weihs, T. P.; Hodgin, R.; Wilkins, P.; May, C. Rapid Initiation of Reactions in Al/Ni Multilayers with Nanoscale Layering. *J. Phys. Chem. Solids* **2010**, *71*, 84−89.

(8) Jian, G.; Liu, L.; Zachariah, M. R. Facile Aerosol Route to Hollow CuO Spheres and Its Superior Performance as an Oxidizer in

Nanoenergetic Gas Generators. *Adv. Funct. Mater.* **2012**, *23*, 1341−1346.
(9) Martirosyan, K. S.; Wang, L.; Luss, D. Novel Nanoenergetic System Based on Iodine Pentoxide. *Chem. Phys. Lett.* **2009**, *483*, 107−110.
(10) Churaman, W. A.; Currano, L. J.; Morris, C. J.; Rajkowski, J. E.; Bergbreiter, S. The First Launch of an Autonomous Thrust-Driven Microrobot Using Nanoporous Energetic Silicon. *J. Microelectromech. Syst.* **2012**, *21*, 198−205.
(11) Korampally, M.; Apperson, S. J.; Staley, C. S.; Castorena, J. A.; Thiruvengadathan, R.; Gangopadhyay, K.; Mohan, R. R.; Ghosh, A.; Polo-Parada, L.; Gangopadhyay, S. Transient Pressure Mediated Intranuclear Delivery of FITC-Dextran into Chicken Cardiomyocytes by MEMS-Based Nanothermite Reaction Actuator. *Sens. Actuators, B* **2012**, *171−172*, 1292−1296.
(12) Stamatis, D.; Jiang, X.; Beloni, E.; Dreizin, E. L. Aluminum Burn Rate Modifiers Based on Reactive Nanocomposite Powders. *Propellants, Explos., Pyrotech.* **2010**, *35*, 260−267.
(13) Reese, D. A.; Groven, L. J.; Son, S. F.; Mukasyan, A. S. *47th AIAA/ASME/SAE/ASEE Joint Propulsion Conference & Exhibit*, San Diego, CA, USA 31 July−03 August, 2011.
(14) Lee, C. H.; Jeong, T. H.; Kim, D. K.; Jeong, W. H.; Kang, M.-K.; Hwang, T. H.; Kim, H. J. Crystallization of Amorphous Silicon Thin Films Using Nanoenergetic Intermolecular Materials with Buffer Layers. *J. Cryst. Growth* **2009**, *311*, 1025−1031.
(15) Bae, J. H.; Kim, D. K.; Jeong, T. H.; Kim, H. J. Crystallization of Amorphous Si Thin Films by the Reaction of MoO_3/Al Nano-engineered Thermite. *Thin Solid Films* **2010**, *518*, 6205−6209.
(16) Grinshpun, S. A.; Adhikari, A.; Yermakov, M.; Reponen, T.; Dreizin, E.; Schoenitz, M.; Hoffmann, V.; Zhang, S. Inactivation of Aerosolized Bacillus Atrophaeus (BG) Endospores and MS2 Viruses by Combustion of Reactive Materials. *Environ. Sci. Technol.* **2012**, *46*, 7334−7341.
(17) Feng, J.; Jian, G.; Liu, Q.; Zachariah, M. R. Passivated Iodine Pentoxide Oxidizer for Potential Biocidal Nanoenergetic Applications. *ACS Appl. Mater. Interfaces* **2013**, *5*, 8875−8880.
(18) Pantoya, M. L.; Granier, J. J. Combustion Behavior of Highly Energetic Thermites: Nano versus Micron Composites. *Propellants, Explos., Pyrotech.* **2005**, *30*, 53−62.
(19) Weismiller, M. R.; Malchi, J. Y.; Lee, J. G.; Yetter, R. A.; Foley, T. J. Effects of Fuel and Oxidizer Particle Dimensions on the Propagation of Aluminum Containing Thermites. *Proc. Combust. Inst.* **2011**, *33*, 1989−1996.
(20) Blobaum, K. J.; Reiss, M. E.; Plitzko, J. M.; Weihs, T. P. Deposition and Characterization of a Self-Propagating CuOx/Al Thermite Reaction in a Multilayer Foil Geometry. *J. Appl. Phys.* **2003**, *94*, 2915−2922.
(21) Petrantoni, M.; Rossi, C.; Salvagnac, L.; Conédéra, V.; Estève, A.; Tenailleau, C.; Alphonse, P.; Chabal, Y. J. Multilayered Al/CuO Thermite Formation by Reactive Magnetron Sputtering: Nano versus Micro. *J. Appl. Phys.* **2010**, *108*, 084323.
(22) Kuntz, J. D.; Cervantes, O. G.; Gash, A. E.; Munir, Z. A. Tantalum−Tungsten Oxide Thermite Composites Prepared by Sol−Gel Synthesis and Spark Plasma Sintering. *Combust. Flame* **2010**, *157*, 1566−1571.
(23) Tillotson, T. M.; Gash, A. E.; Simpson, R. L.; Hrubesh, L. W.; Jr, J. H. S.; Poco, J. F. Nanostructured Energetic Materials Using Sol−Gel Methodologies. *J. Non-Cryst. Solids* **2001**, *285*, 338−345.
(24) Dreizin, E. L.; Schoenitz, M. Nano-Composite Energetic Powders Prepared by Arrested Reactive Milling. US Patent 7,524,355 B2, Apr. 28, 2009.
(25) Badiola, C.; Schoenitz, M.; Zhu, X.; Dreizin, E. L. Nano-composite Thermite Powders Prepared by Cryomilling. *J. Alloys Compd.* **2009**, *488*, 386−391.
(26) Malchi, J. Y.; Foley, T. J.; Yetter, R. A. Electrostatically Self-Assembled Nanocomposite Reactive Microspheres. *ACS Appl. Mater. Interfaces* **2009**, *1*, 2420−2423.
(27) Séverac, F.; Alphonse, P.; Estève, A.; Bancaud, A.; Rossi, C. High-Energy Al/CuO Nanocomposites Obtained by DNA-Directed Assembly. *Adv. Funct. Mater.* **2012**, *22*, 323−329.
(28) Becker, C. R.; Apperson, S.; Morris, C. J.; Gangopadhyay, S.; Currano, L. J.; Churaman, W. A.; Stoldt, C. R. Galvanic Porous Silicon Composites for High-Velocity Nanoenergetics. *Nano Lett.* **2011**, *11*, 803−807.
(29) Plummer, A.; Kuznetsov, V.; Joyner, T.; Shapter, J.; Voelcker, N. H. The Burning Rate of Energetic Films of Nanostructured Porous Silicon. *Small* **2011**, *7*, 3392−3398.
(30) Zhang, K.; Rossi, C.; Ardila Rodriguez, G. A.; Tenailleau, C.; Alphonse, P. Development of a Nano-Al/CuO Based Energetic Material on Silicon Substrate. *Appl. Phys. Lett.* **2007**, *91*, 113117.
(31) Xu, D.; Yang, Y.; Cheng, H.; Li, Y. Y.; Zhang, K. Integration of Nano-Al with Co_3O_4 Nanorods to Realize High-Exothermic Core−Shell Nanoenergetic Materials on a Silicon Substrate. *Combust. Flame* **2012**, *159*, 2202−2209.
(32) Apperson, S.; Shende, R. V.; Subramanian, S.; Tappmeyer, D.; Gangopadhyay, S.; Chen, Z.; Gangopadhyay, K.; Redner, P.; Nicholich, S.; Kapoor, D. Generation of Fast Propagating Combustion and Shock Waves with Copper Oxide/Aluminum Nanothermite Composites. *Appl. Phys. Lett.* **2007**, *91*, 243109.
(33) Kim, S. H.; Zachariah, M. R. Enhancing the Rate of Energy Release from NanoEnergetic Materials by Electrostatically Enhanced Assembly. *Adv. Mater.* **2004**, *16*, 1821−1825.
(34) Ohkura, Y.; Liu, S.-Y.; Rao, P. M.; Zheng, X. Synthesis and Ignition of Energetic CuO/Al Core/Shell Nanowires. *Proc. Combust. Inst.* **2011**, *33*, 1909−1915.
(35) Petrantoni, M.; Rossi, C.; Conédéra, V.; Bourrier, D.; Alphonse, P.; Tenailleau, C. Synthesis Process of Nanowired Al/CuO Thermite. *J. Phys. Chem. Solids* **2010**, *71*, 80−83.
(36) Yan, S.; Jian, G.; Zachariah, M. R. Electrospun Nanofiber-Based Thermite Textiles and Their Reactive Properties. *ACS Appl. Mater. Interfaces* **2012**, *4*, 6432−6435.
(37) Zhou, X.; Xu, D.; Zhang, Q.; Lu, J.; Zhang, K. Facile Green in situ Synthesis of Mg/CuO Core/Shell Nanoenergetic Arrays with Superior Heat Release Property and Long-Term Storage Stability. *ACS Appl. Mater. Interfaces* **2013**, *5*, 7641−7646.
(38) Menon, L.; Patibandla, S.; Ram, K. B.; Shkuratov, S. I.; Aurongzeb, D.; Holtz, M.; Berg, J.; Yun, J.; Temkin, H. Ignition Studies of Al/Fe_2O_3 Energetic Nanocomposites. *Appl. Phys. Lett.* **2004**, *84*, 4735−4737.
(39) Knepper, R.; Snyder, M. R.; Fritz, G.; Fisher, K.; Knio, O. M.; Weihs, T. P. Effect of Varying Bilayer Spacing Distribution on Reaction Heat and Velocity in Reactive Al/Ni Multilayers. *J. Appl. Phys.* **2009**, *105*, 083504.
(40) Fischer, S. H.; Grubelich, M. C. *Proceedings of the 24th International Pyrotechics Seminar*, Monterey, CA, USA July 27−31, 1998.
(41) Moore, K.; Pantoya, M. L. Combustion of Environmentally Altered Molybdenum Trioxide Nanocomposites. *Propellants, Explos., Pyrotech.* **2006**, *31*, 182−187.
(42) In *CRC Handbook of Chemistry and Physics*, Internet Version 2005; Lide, D. R., Ed.; CRC Press: Boca Raton, FL, 2005.
(43) Apperson, S. J.; Bezmelnitsyn, A. V.; Thiruvengadathan, R.; Gangopadhyay, K.; Gangopadhyay, S.; Balas, W. A.; Anderson, P. E.; Nicolich, S. M. Characterization of Nanothermite Material for Solid-Fuel Microthruster Applications. *J. Propul. Power* **2009**, *25*, 1086−1091.
(44) Ardila Rodríguez, G. A.; Suhard, S.; Rossi, C.; Estève, D.; Fau, P.; Sabo-Etienne, S.; Mingotaud, A. F.; Mauzac, M.; Chaudret, B. A Microactuator Based on the Decomposition of an Energetic Material for Disposable Lab-on-Chip Applications: Fabrication and Test. *J. Micromech. Microeng.* **2009**, *19*, 015006.
(45) Park, K.-C.; Choi, H. J.; Chang, C.-H.; Cohen, R. E.; McKinley, G. H.; Barbastathis, G. Nanotextured Silica Surfaces with Robust Superhydrophobicity and Omnidirectional Broadband Supertransmissivity. *ACS Nano* **2012**, *6*, 3789−3799.

(46) Liu, K.; Jiang, L. Bio-Inspired Self-Cleaning Surfaces. *Annu. Rev. Mater. Res.* **2012**, *42*, 231−263.
(47) Quéré, D. Wetting and Roughness. *Annu. Rev. Mater. Res.* **2008**, *38*, 71−99.
(48) Robbie, K.; Brett, M. J.; Lakhtakia, A. Chiral Sculptured Thin Films. *Nature* **1996**, *384*, 616.
(49) Zhang, K.; Rossi, C.; Tenailleau, C.; Alphonse, P. Aligned Three-Dimensional Prismlike Magnesium Nanostructures Realized onto Silicon Substrate. *Appl. Phys. Lett.* **2008**, *92*, 063123.
(50) Zhang, Y.; Yang, G. H.; Kang, E. T.; Neoh, K. G.; Huang, W.; Huan, A. C. H.; Wu, S. Y. Deposition of Fluoropolymer Films on Si (100) Surfaces by Rf Magnetron Sputtering of Poly-(tetrafluoroethylene). *Langmuir* **2002**, *18*, 6373−6380.
(51) Starkweather, H. W.; Ferguson, R. C.; Chase, D. B.; Minor, J. M. Infrared Spectra of Amorphous and Crystalline Poly-(tetrafluoroethy1ene). *Macromolecules* **1985**, *18*, 1684−1686.
(52) Biederman, H.; Zeuner, M.; Zalman, J.; Bílková, P.; Slavínská, D.; Stelmasuk, V.; Boldyreva, A. Rf Magnetron Sputtering of Polytetrafluoroethylene under Various Conditions. *Thin Solid Films* **2001**, *392*, 208−213.
(53) Chen, W.; Fadeev, A. Y.; Hsieh, M. C.; Didem, O.; Youngblood, J.; Mccarthy, T. J. Ultrahydrophobic and Ultralyophobic Surfaces: Some Comments and Examples. *Langmuir* **1999**, *15*, 3395−3399.
(54) Osborne, D. T.; Pantoya, M. L. Effect of Al Particle Size on the Thermal Degradation of Al/Teflon Mixtures. *Combust. Sci. Technol.* **2007**, *179*, 1467−1480.
(55) Sippel, T. R.; Son, S. F.; Groven, L. J. Altering Reactivity of Aluminum with Selective Inclusion of Polytetrafluoroethylene through Mechanical Activation. *Propellants, Explos., Pyrotech.* **2013**, *38*, 286−295.
(56) Son, S. F.; Asay, B. W.; Foley, T. J.; Yetter, R. A.; Wu, M. H.; Risha, G. A. Combustion of Nanoscale Al/MoO_3 Thermite in Microchannels. *J. Propul. Power* **2007**, *23*, 715−721.
(57) Dutro, G. M.; Yetter, R. A.; Risha, G. A.; Son, S. F. The Effect of Stoichiometry on the Combustion Behavior of a Nanoscale Al/MoO_3 Thermite. *Proc. Combust. Inst.* **2009**, *32*, 1921−1928.
(58) Weismiller, M. R.; Malchi, J. Y.; Yetter, R. A.; Foley, T. J. Dependence of Flame Propagation on Pressure and Pressurizing Gas for an Al/CuO Nanoscale Thermite. *Proc. Combust. Inst.* **2009**, *32*, 1895−1903.
(59) Levitas, V. I.; Asay, B. W.; Son, S. F.; Pantoya, M. Melt Dispersion Mechanism for Fast Reaction of Nanothermites. *Appl. Phys. Lett.* **2006**, *89*, 071909.
(60) Levitas, V. I.; Asay, B. W.; Son, S. F.; Pantoya, M. Mechanochemical Mechanism for Fast Reaction of Metastable Intermolecular Composites Based on Dispersion of Liquid Metal. *J. Appl. Phys.* **2007**, *101*, 083524.